Article

The Amorphous Carbon Thin Films Synthesized by Gas Injection Magnetron Sputtering Technique in Various Gas Atmospheres

Rafal Chodun [1,*], Lukasz Skowronski [2], Marek Trzcinski [2], Katarzyna Nowakowska-Langier [3], Krzysztof Kulikowski [1], Mieczyslaw Naparty [2], Michal Radziszewski [1] and Krzysztof Zdunek [1]

[1] Faculty of Materials Science and Engineering, Warsaw University of Technology, Woloska 141 St., 02-507 Warsaw, Poland
[2] Institute of Mathematics and Physics, Bydgoszcz University of Science and Technology, Al. Prof. S. Kaliskiego 7 St., 85-796 Bydgoszcz, Poland
[3] National Centre for Nuclear Research, Andrzeja Soltana 7, 05-400 Otwock-Swierk, Poland
* Correspondence: rafal.chodun@pw.edu.pl

Abstract: This work presents the potential for using pulsed gas injection to produce amorphous carbon films. In this experiment, the frequency of injecting small amounts of gas was used to control the pressure amplitudes, thus achieving the conditions of plasma generation from stationary, through quasi-stationary, to pulsed oscillations of pressure. In addition, we used various gases and their mixtures, an alternative to argon. In the experiment, we studied the energy state of the plasma. The films were examined for phase and chemical composition, surface morphology, and optical and mechanical properties. We determined low-frequency pulsed gas injections to be conditions favorable for $C(sp^3) - C(sp^3)$ bond formation. The plasma generated by gas injections is better ionized than that generated by static pressure. Pulsed conditions favor the plasma species to retain their kinetic energy, limiting the probability of intermolecular collision events. Since helium has a relatively high ionization energy, it is a practical addition to sputtering gas because of the increasing sp^3 content in the films. The electrons created by helium ionization improve the plasma's ionization degree.

Keywords: amorphous carbon; a-C; diamond-like carbon; DLC; magnetron sputtering; gas injection; GIMS; Raman spectroscopy; optical properties; nanohardness

1. Introduction

Amorphous carbon (a-C) coatings attract the community's attention with exciting properties. Among them are high hardness, good wear resistance, low friction coefficient, transparency, wide band gap, chemical inertness, and biocompatibility [1–3]. Thanks to these properties, amorphous carbon layers are of great interest from the application side: tools, photovoltaics, electronics, photonics, biomedical engineering, etc. [4–10]. The a-C films consist of a mixture of carbon phases with sp^2 and sp^3 hybridization. The sp^3/sp^2 fraction depends on the deposition conditions and determines the material properties of the coating [11,12]. The range of a-C properties is thus extensive, from coatings with graphite-like properties to diamond-like ones. This is an additional advantage of these coatings, as it gives the technological possibility to produce layers precisely with specific properties.

Forming a metastable $C(sp^3) - C(sp^3)$ bond configuration in carbon is difficult due to the high nucleation barrier of diamonds [13]. It is conventionally achieved by applying heat and pressure work. Unconventional approaches use, among other means, the work of an electric field [14]. Among the technological ways of performing unconventional synthesis are the methods of Plasma Surface Engineering [15,16].

Magnetron sputtering (MS) is one of the most popular PVD methods for layer fabrication. Its advantages are versatility, high flexibility in the types of fabricated coatings,

chemical purity, homogeneity, and scalability for industrial production [17,18]. Magnetron sputtering, in its conventional direct current MS (dcMS) variant, is characterized by a relatively low degree of ionization of only a few percent, with plasma particle energies reaching only a few eV [19,20]. This makes the a-C layers produced by dcMS have graphite-like features [21,22]. MS technology is being intensively improved, and one of the leading development paths is to take advantage of the benefits of highly ionized plasmas. One variety of MS using high-energy plasma is High Power Impulse Magnetron Sputtering (HiPIMS). In this technique, the plasma is excited in a high-current discharge, its degree of ionization reaches several tens of percent, and the plasma particles reach energies of 100 eV [23–25]. As a result, the a-C layers are characterized by an effective content of $C(sp^3) - C(sp^3)$ bonds and, thus, diamond-like features [26–30].

Another way to increase plasma particle energy is represented by the Gas Injection Magnetron Sputtering (GIMS) technique. The GIMS technique is a pulsed technique that generates discrete plasma streams (plasma pulses) in an environment of dynamically varying working gas concentration, controlled by high-speed pulsed gas valves [31,32]. Typically, in GIMS, layers are produced due to the generation of 10–10^2 ms plasma pulses at frequencies of 10^{-1}–10^1 Hz. The pulse power density is of the order of 10^2 W/cm^2. Despite the relatively high power density, the pulsed operation makes the condition for the film's growth at room temperature [33].

GIMS is a practical implementation of the idea of increasing the energy of plasmoids, not as a result of using high-power sources (HiPIMS), but by carrying out the process of deposition under conditions limiting energy dissipation. This is performed by the pulsed method of distributing small portions of gas and using efficient vacuum pumps. Each generated pulse of plasma spreads in a volume of relatively low pressure compared to the MS process at constant pressure. Such conditions favor the preservation of high energies of plasma particles. So far, we have been able to confirm the effectiveness of the GIMS technique:

(1) By recording the optical emission spectroscopy OES spectra showing high-energy plasma components in GIMS [31,32];
(2) By recording the effects of the interaction of the energetic GIMS plasma with the substrate surface [31];
(3) By depositing phases on substrates whose nucleation is characteristic of high-energy phase equilibrium conditions [34–37];
(4) By depositing non-stoichiometric phases on substrates [38,39].

The advantages of GIMS led it to be implemented in the industry in producing coatings on large-scale, 3 m × 2 m, glass [40,41]. The layers produced on glass using the GIMS technique exhibited better adhesion and uniformity than the standard magnetron sputtering version.

This work aimed to study the GIMS technique's effects in fabricating a-C coatings. We believed that this technique could be particularly effective in obtaining an increased sp^3 phase content in the a-C layers. The performance characteristics of the GIMS technique substantiate this assumption. As part of our experiment, we took advantage of the ability to electronically control the operating parameters of the pulsed valves to produce various coating fabrication conditions. The a-C coatings were produced under dynamically fluctuating pressure conditions and quasi-stationary conditions. We also used non-standard gases and their mixtures in our experiment.

Our research procedure characterized the a-C layer synthesis environment and the coatings from structural, phase, and chemical perspectives. In order to obtain a complementary characterization, we studied the properties of the produced layers.

2. Materials and Methods

2.1. Apparatus

The a-C coatings synthesis was carried out in a vacuum apparatus presented in Figure 1. The vacuum chamber had a vacuum pump system consisting of turbomolecular, roots, and rotary pumps. The vacuum pump unit could reach a 5×10^{-3} Pa base pressure. According to the Gencoa criterion [42], a highly unbalanced circular magnetron was used as the plasma source. The 50 mm diameter pyrolytic graphite targets were installed in the magnetron. Figure 1a shows a diagram of an apparatus for synthesizing layers in an argon atmosphere dosed by a single pulse valve into the glow discharge zone above the surface of a graphite target. The operation of the pulse gas valve GV is controlled by a controller coupled to the power supply (PS) of the magnetron gun. The first part of our experiment involved changing the gas dosing frequency parameter. We changed this parameter to the 0.2–1 Hz range in our experiment. In this way, we created conditions for more to less dynamic pressure changes, periodically repetitive with the operation of the pulse valve. Considering the pumping system's limited efficiency, the relatively higher gas dosing frequency (1 Hz) variant created quasi-stationary pressure conditions. The variant of a relatively low gas metering frequency (0.2 Hz) generated highly fluctuating pressure conditions. The qualitative difference between these variants is presented in Figure 1b. The pressure characteristics presented are illustrative. A precise determination of the oscillation was impossible due to the high time inertia of the used vacuum gauge. Pawlak [43] studied a more accurate study of the pressure characteristic in GIMS.
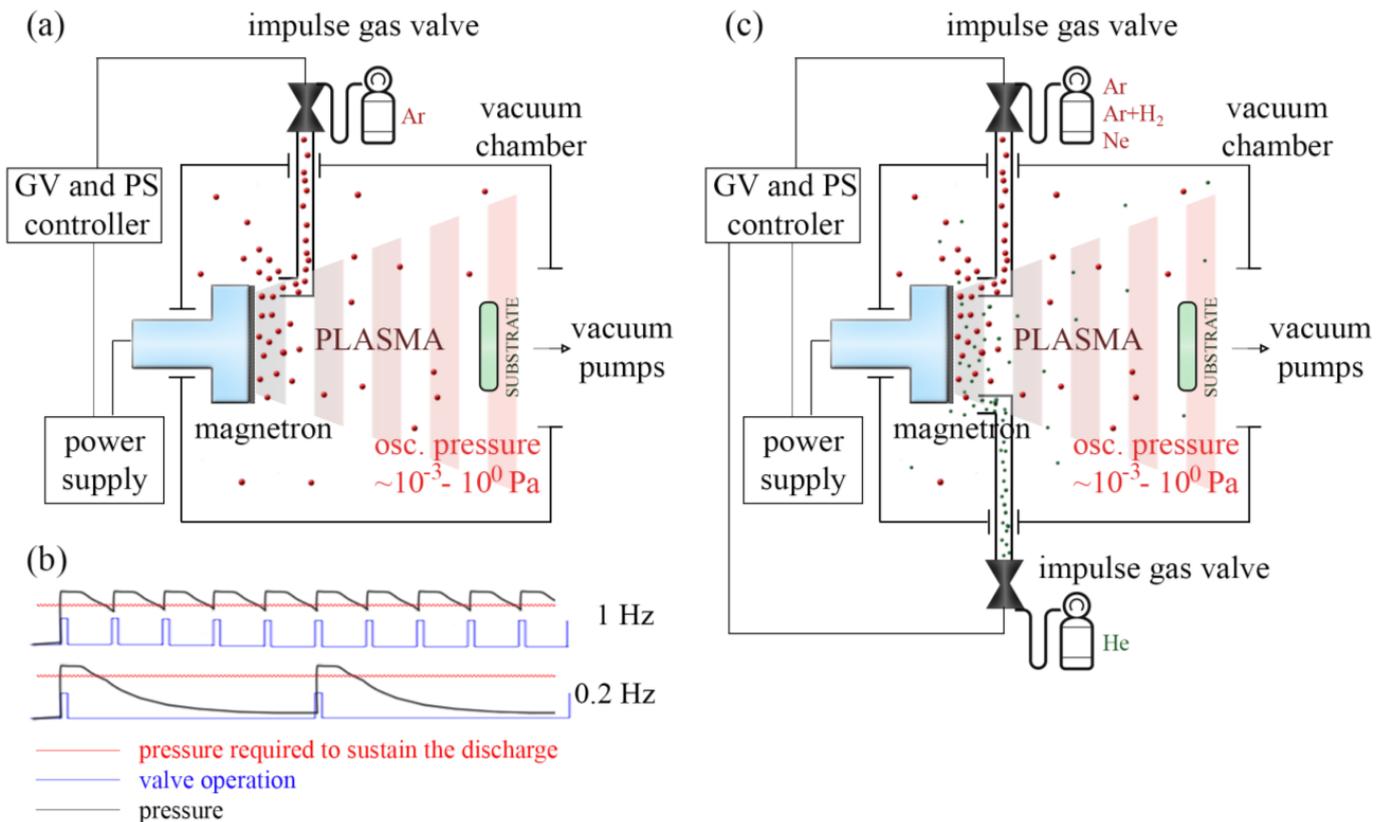
Figure 1. Diagram illustrating: (**a**) the apparatus configuration for a-C films deposition in Ar atmosphere controlled by a single pulse valve, (**b**) oscillations depending on the frequency of impulse valve operation, (**c**) the apparatus configuration for a-C films deposition in various gas atmospheres controlled by two pulsed valves.

The second part of the experiment investigated the effects of performing deposition processes in different gaseous atmospheres. For this purpose, two independently controlled pulse valves were used—see Figure 1c.

2.2. Coatings Synthesis Processes

The coating deposition processes were carried out using Ar, Ar + H_2 (5% H_2), Ne, and He gases (N5.0 purity). The working atmosphere was created with injections from a fast pulse valve directly at the target surface. The pressure at the valve inlet was set to 1.5×10^5 Pa. In the first part of the experiment, the opening time of the valve was fixed at 1 ms to maintain as low-pressure conditions as possible. Ar gas was distributed to the glow discharge region of the magnetron gun with various frequencies, 0.2–1 Hz.

Additionally, a referencing a-C film was fabricated in the conditions of 0.4 Pa constant pressure by the Pulsed Magnetron Sputtering (PMS) technique. This choice is based on the fact that in our GIMS process, the power is distributed as in the PMS mode. The only difference is using a pulse valve that injects gas in a controlled manner. This allowed us to achieve pulsed pressure conditions. The frequency of injections was chosen experimentally. A gas dosing frequency of 0.2 Hz determined conditions where the interval between gas injections was high enough for the pumping system to evacuate gas to a base pressure of 5×10^{-3} Pa. A threshold frequency of 1 Hz determined the quasi-stationary conditions, in which the pressure slightly oscillated around a value of 0.4 Pa. For complete characterization, processes were also carried out at transitional frequencies. The deposition process parameters are summarized in Table 1.

Table 1. Parameters of a-C coatings deposition in Ar atmosphere.

Process	PMS	GIMS 1 Hz	GIMS 0.5 Hz	GIMS 0.(3) Hz	GIMS 0.25 Hz	GIMS 0.2 Hz
Valve frequency (Hz)	-	1	0.5	0.(3)	0.25	0.2
Time of valve opening (ms)	-			1		
Pressure (Pa)	0.4			-		
Pulse of power duration (ms)	-			100		
Deposition time (min)	3	30	60	90	120	150

The second part of the experiment examined the effects of using various gases and their mixtures in the synthesizing a-C layers. The a-C layers were fabricated in Ar, Ne, and Ar + H_2 atmospheres. In addition, He was used as a component of the base gas mixtures. For the pressure conditions to be reproducible, the sum of the opening times of a single valve or two valves was 2 ms. The process parameters are summarized in Table 2.

Table 2. Parameters of a-C coatings deposition in various gas atmospheres.

Gas 1	Ar		Ar + H_2		Ne	
Gas 2	-	He	-	He	-	He
Time of valve opening (ms)	2 (Ar)	1 (Ar) 1 (He)	2 (Ar + H_2)	2 (Ar + H_2) 1 (He)	2 (Ne)	2 (Ne) 1 (He)
Valve frequency (Hz)			0.2			
Pulse of power duration (ms)			100			
Deposition time (min)			150			

The n-type 100 silicon substrates were prepared by ultrasonic cleaning in acetone and drying. After that, they were located perpendicularly to the magnetron Z-axis at 10 cm from its surface. The substrate stage was electrically grounded during coating deposition with the magnetron anode and vacuum chamber. The magnetron system was powered using a Dora Power Systems pulsed DC power supply with a carrier frequency of 125 kHz [44,45].

2.3. Plasma Characterization

The current and voltage waveforms of the magnetron power circuit were collected to characterize the discharge. The power waveforms were calculated from the current and voltage characteristics, measured using the 1 A: 0.1 V Rogowski coil and 1 kV: 1 V voltage, and registered by a Rigol oscilloscope. The pulse energy was calculated using the integral over time. All the calculations were made using the Origin Lab software.

The OES measurements were obtained using an Optel energy-dispersive optical spectrometer at a 200–900 nm wavelength. The signals were collected through a quartz window and an optical fiber. The exposition time was set to a full single plasma pulse. During these experiments, the optical collimator was perpendicular to the magnetron *Z*-axis and placed 55 mm from the cathode surface.

2.4. Coatings Characterization

The Raman scattering of the a-C films was studied using a 532 nm VIS laser (2.33 eV) and a 266 nm UV laser (4.66 eV) as the source of VIS and UV excitation, an Ar+ laser and the Crylas FQCW266-50 diode-pumped continuous wave solid-state laser was used, respectively. The scattered light was dispersed by a JASCO NRS 5100 spectrometer working in backscattering mode. The laser beams were focused onto ~15 μm spots during the measurements. The parameters of the spectra registration were optimized based on the excellent peak intensity. No visible damage to the surface of the samples was observed after the Raman examination. In order to analyze the registered spectra, they were processed using the JASCO peak processing software. During the processing, the spectra were interpolated and their background was subtracted to realign the intensity levels at each side of the presented range. The curve fitting procedure included the determination of the peaks *D* and *G* position and a full width at half maximum FWHM. The final intensities, positions, FWHM, and the shapes (Gaussian, Lorenztian, or a mixed Gaussian—Lorentzian function) of any elementary components were optimized by curve fitting software using a least-squares method. The $C(sp^3) - C(sp^3)$ bond content was evaluated based on the *G* peak parameters: *G* peak FWHM and *G* peak dispersion rate [46]. The sp^3/sp^2 ratio as the *G* peak dispersion is expressed by:

$$sp^3 content = -0.07 + 2.5 \cdot Disp(G), \tag{1}$$

where:

$$Disp(G) = \left| \frac{Pos(G)@\lambda_2 - Pos(G)@\lambda_1}{\lambda_2 - \lambda_1} \right|, \tag{2}$$

$Pos(G)@\lambda_2$ and $Pos(G)@\lambda_1$ are the *G* peak positions at λ_2 and λ_1 irradiation, respectively. λ_2 and λ_1 are the laser wavelength.

The sp^3/sp^2 ratio as the FWHM criterion can be calculated from:

$$sp^3 content = -0.25 + 1.9 \cdot 10^{-2} \cdot W - 3.01 \cdot 10^{-5} \cdot W^2, \tag{3}$$

where:

$$W = FWHM(G) + 0.21 \cdot (514 - \lambda), \tag{4}$$

and λ is the laser wavelength.

In order to investigate the respective contribution of the sp^2 and sp^3 hybridization bonds in the near-surface layers of the samples, an X-ray Photoelectron Spectroscopy (XPS) analysis was performed. Measurements were made under ultra-high vacuum conditions (base pressure $\leq 2 \cdot 10^{-10}$ mbar). The excitation radiation source was an Al Kα lamp (1486.6 eV), and the angle of incidence of the excitation beam was 55 degrees. Photoelectron energy was recorded using the VG-Scienta R3000 analyzer. The energy step was set to $\Delta E = 100$ meV. Experimental data were fitted using CasaXPS software using the Shirley background and Gauss-Lorentz line shapes. The C1's level was deconvoluted into four components, the main two related to the $C(sp^2) - C(sp^2)$ and $C(sp^3) - C(sp^3)$ bonds, and

two other peaks at higher binding energies from the hydroxyl (C–O) and carboxylic (C=O) bonds from surface impurities.

The AFM measurements were performed using the Innova device from Bruker. The tapping mode was used to investigate the surface topography of the fabricated carbon films. The scan size was 1 μm × 1 μm. The analysis was performed using the Gwyddion software.

The nanohardness measurements were carried out using Vantage Alpha Nanotester (Micromaterials Ltd., UK) equipment. A maximum load of 0.5 mN, loading time of 10 s, dwell period of 5 s, and 10 s unloading time were applied. For every sample, 25 indentations were performed, and the mean values, with standard deviation, were calculated.

The ellipsometric azimuths Ψ and Δ have been recorded in the spectral range from 0.6 eV (2000 nm) to 6.5 eV (190 nm) for three angles of incidence 65°, 70°, and 75°. The measurements were performed using the V-VASE device from J.A.Woollam Co., Inc. (Lincoln, NE, USA).

3. Results and Discussion

Figure 2 shows the power pulse characteristics of the GIMS processes and the characteristics of the MS process under constant pressure conditions. The power pulses were integrated to calculate their energies. In each case, the integration constant was 100 ms. The plot shows that the conditions of the low frequency of gas injection favor plasma generation with higher energy. This is especially evident in the initial stage of the discharge. In our opinion, the amount of energy released during the discharge is influenced by (1) the pressure and (2) the size of the injected gas portion. The favorable conditions for obtaining and sustaining a relatively highly ionized discharge are low pressure in the chamber and a relatively high portion of injected gas. Low chamber pressure limits the dissipation of kinetic energy during collisions of energetic plasma species. The size of the gas portion represents a population of potential particles that can be ionized. The best conditions for a high-energy discharge are those during gas injection.

In our experimental setup, the valve was located outside the vacuum chamber. The gas was delivered via a tube with a diameter of 1 mm and a length of about 200 mm. This makes the gas injection inertially executed. The discharge delay to the start of the valve was 12 ms and, at its beginning, a high amount of gas enters the discharge zone, the concentration of which decreases with time. At the same time, the pressure in the chamber increases as a result of filling it with injected gas. By this, we observe a decrease in the energy of the discharge during the pulse.

Nevertheless, a strong current discharge can be observed at the beginning of the pulse generated at lower pressure conditions. The discharge has a higher energy when lower pressure conditions are achieved in the chamber. Such conditions occur when the process is carried out at a low frequency of gas injection—see Figure 1b. This difference can be seen when comparing the PMS stationary or quasi-stationary GIMS 1 Hz process with the GIMS 0.2 Hz process.

OES studies also showed a qualitative difference between the plasma generation processes under PMS stationary and the GIMS pulsed conditions. Figure 3 shows the recorded OES spectra in the visible VIS and UV ranges. The spectral ranges of excited Ar I particles, Ar II ions, and sputtered C I excited carbon particles were selected. Due to the relatively low resolution of the spectrometer and the slight differences in the lines intensity of all the GIMS processes, it is not possible to make a quantitative assessment of the population size of the individual excited plasma species. Nevertheless, there is a qualitative difference between the intensity of the OES spectrum of the PMS process and the GIMS processes, which may be related to the higher degree of ionization of the plasma produced by the GIMS. The presence of Ar II ions in the OES spectrum of the GIMS processes can also demonstrate this. It seems that the OES results are reflected in the energy state of the plasma pulses determined from the power characteristics of the magnetron power system. The differences in the plasma state seem significant enough that we would expect them to affect the characteristics of the a-C films fabricated under these conditions.
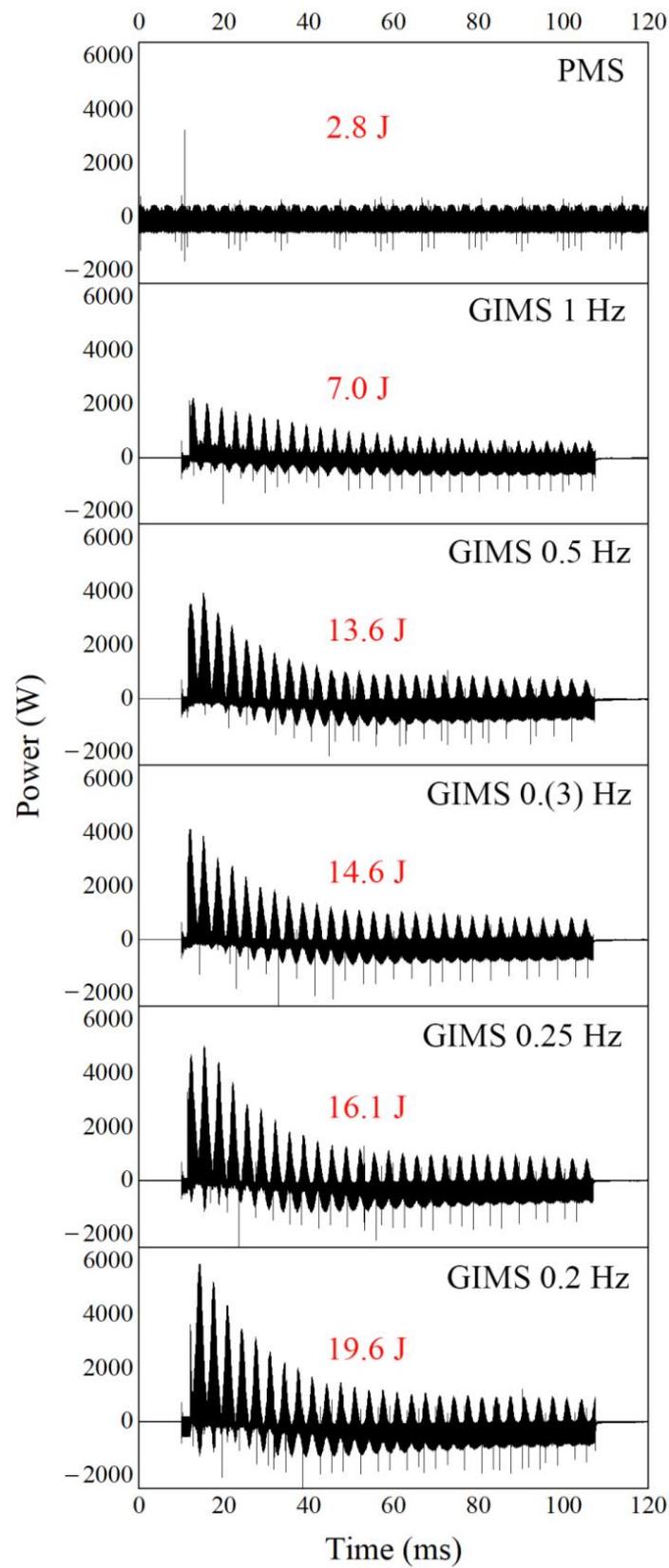
Figure 2. The power characteristics measured in the electric circuit of the magnetron gun operating in PMS and various GIMS conditions. The graphs are labeled with the energy values of the entire single power pulses.
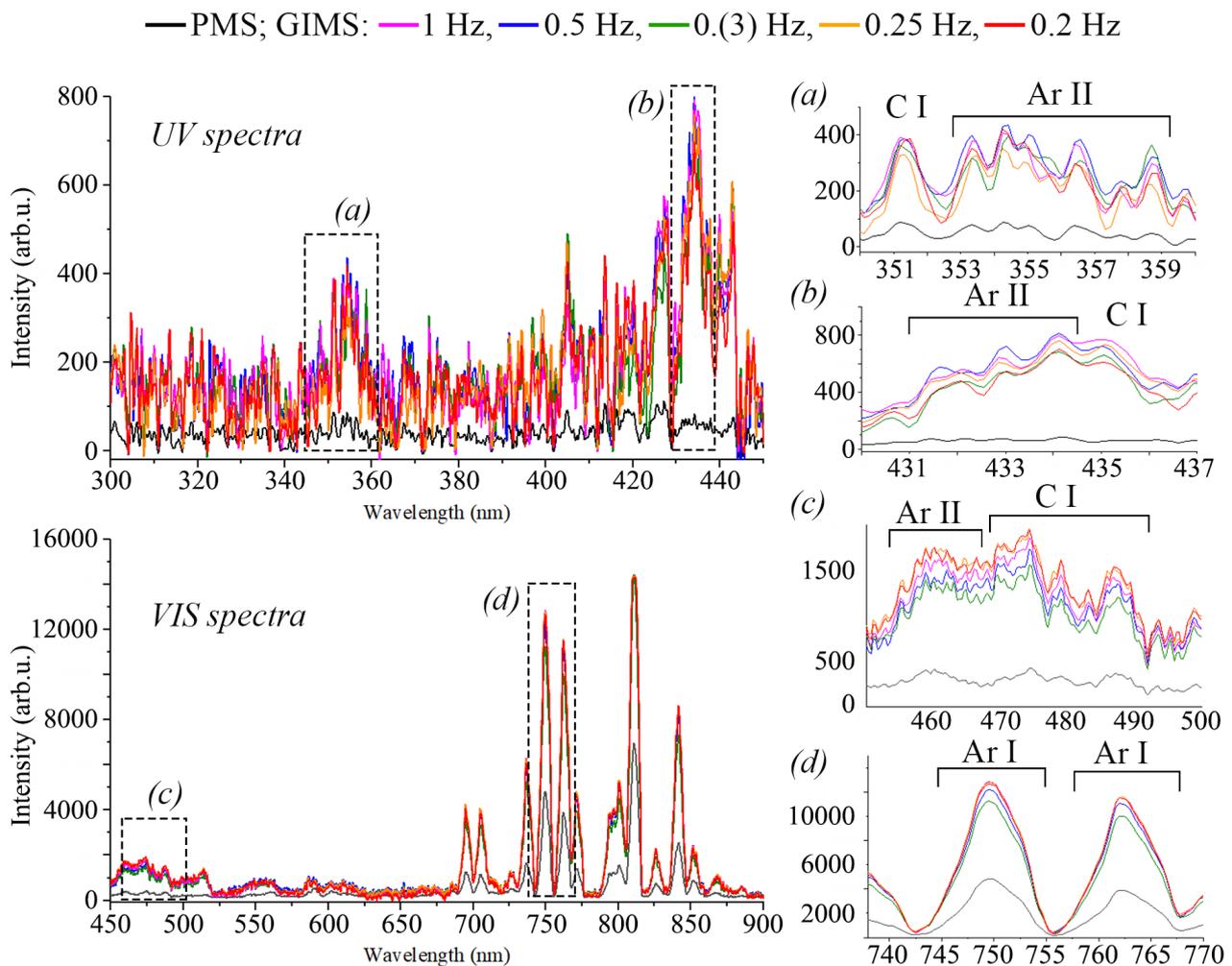
Figure 3. UV (**top left**) and VIS (**bottom left**) OES plasma spectra generated in PMS and various GIMS conditions. Selected ranges of the OES spectrum of the characteristic groups of plasma constituents occurrence (**right column**).

Figure 4 shows the Raman spectra of the a-C layers produced under different Ar dosing conditions. The spectra were recorded under VIS and UV laser irradiation. The measured spectra were fitted with two elementary *D* and *G* spectra. The *G* and *D* peaks parameters are shown in Table 3.

Single crystal graphite shows a Raman active band E_{2g}, labeled as *G* (Graphite), at ~1580 cm^{-1}. The *G* peak is assigned to the stretching vibration of the sp^2 sites. With the graphite amorphization, an extra mode A_{1g} appears at ~1350 cm^{-1}, known as the *D* peak (Disorder). The *D* mode is attributed to the breathing modes of the sp^2 sites in rings. The elementary spectrum of peak *D* is slightly shifted towards higher values of cm^{-1} [47]. We think an additional vibrational mode between peaks *D* and *G*, which was not considered when fitting the spectrum, may be responsible for this. We believe that 1400–1450 cm^{-1} $C = C$ polyenic vibrations are very likely [48]. According to the Ferrari diagram of 3-stage carbon amorphization [49], the $C(sp^3) - C(sp^3)$ bond is expected when in-plane correlation length L_s is below 2 nm [50]. Correctly determining the characteristics of the *G* and *D* peaks (positions, intensity, and FWHM) from the DLC Raman spectra is reported as the method of evaluating the $C(sp^3) - C(sp^3)$ bond content. The determined peak parameters are relatively similar. Among the results, the 0.2 Hz GIMS process stands out. In this case, a relatively wide FWHM value of the *G* peak and its significant dispersion were determined. The determined sp^3 content on this basis reached 42% (dispersion criterion)

and 59% (FWHM criterion), respectively. In other cases, the criteria occasionally did not exceed 20% of the sp^3 content.
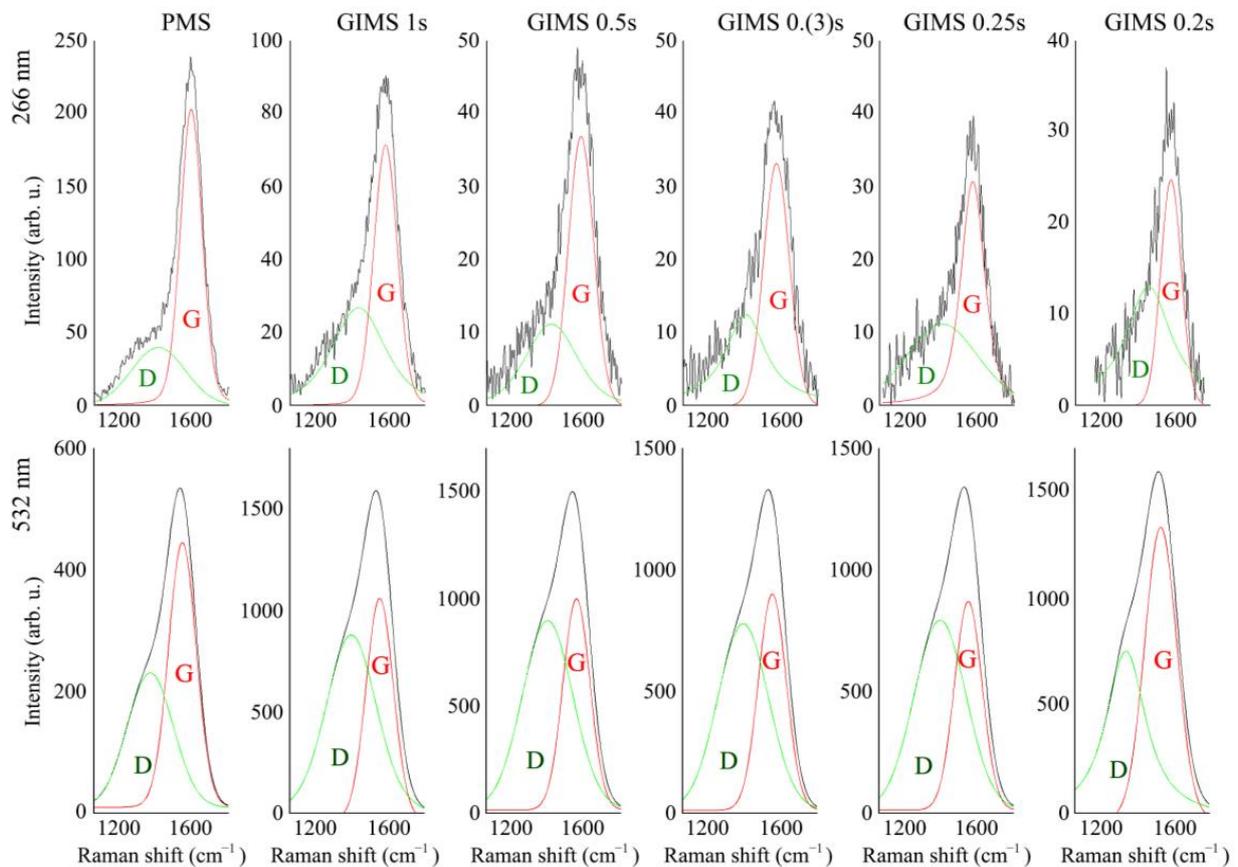
Figure 4. Raman spectra of a-C films fabricated in various conditions of Ar dosing, recorded during the irradiation by 266 nm laser (**top**) and 532 nm laser (**bottom**) and fitted with *D* and *G* elementary spectra.

Raman spectroscopy is a standard method for studying carbon materials because it is susceptible [1]. Nonetheless, it is common practice to supplement this with the XPS method.

In order to confirm the results of the Raman spectroscopy, we examined two a-C layers produced in far conditions, PMS and GIMS 0.2 Hz. The XPS results are shown in Figure 5. Only carbon and oxygen were found in the XPS spectra of all the samples. The material contained no nitrogen or other impurities in detectable concentrations. The C1s peak was slightly broadened towards higher binding energies. Its main component in all samples was a peak attributed to the graphite bonds (sp^2) occurring at an energy of about 284.8 eV. The less intense component associated with the sp^3 hybridization was found at ca. 285.5 eV. At higher binding energies, characteristic peaks were also present, usually attributed to C–O bonds (ca. 286.6 eV) and C=O (288.8 eV).

The oxygen O1s level was fitted with three components. The most intense was around 533.0 eV, attributed to O–C type bonds. A slightly lower peak from the O=C bonds was found at about 531.8 eV. At 534.4 eV, one more component was perhaps related to water molecules on the surface, OH-type bonds, or oxygen molecules adsorbed on the surface. The detailed composition is presented in Table 4.

Table 3. *G* and *D* peak characteristics of Raman spectra of a-C films deposited in various conditions of Ar dosing.

Process	Laser	Peak	Position (cm^{-1})	FWHM (cm^{-1})	Height (arb. u.)	sp^3/sp^2 (*G* Peak Dispersion Criterion) [44]	sp^3/sp^2 (*G* Peak FWHM Criterion) [44]
PMS	266 nm	*G*	1583.88	144.25	201.98	0.19	0.21
		D	1404.25	352.11	39.91		
	532 nm	*G*	1555.44	163.40	390.91		
		D	1389.43	338.13	245.68		
GIMS 1 Hz	266 nm	*G*	1579.84	155.31	71.33	0.20	0.35
		D	1427.54	350.66	26.85		
	532 nm	*G*	1550.16	178.70	10,562.39		
		D	1391.60	338.98	8760.61		
GIMS 0.5 Hz	266 nm	*G*	1574.24	166.14	36.74	0.13	0.33
		D	1407.06	337.76	11.20		
	532 nm	*G*	1552.38	176.35	9912.99		
		D	1391.07	331.55	8964.35		
GIMS 0.(3) Hz	266 nm	*G*	1569.99	168.98	33.09	0.11	0.37
		D	1397.53	273.29	12.37		
	532 nm	*G*	1550.46	181.52	9615.17		
		D	1387.94	331.29	8319.19		
GIMS 0.25 Hz	266 nm	*G*	1569.54	155.49	30.72	0.13	0.37
		D	1390.69	473.23	11.18		
	532 nm	*G*	1548.18	181.00	9862.05		
		D	1391.01	340.68	8964.35		
GIMS 0.2 Hz	266 nm	*G*	1580.48	135.29	24.71	0.42	0.46
		D	1450.91	306.81	13.13		
	532 nm	*G*	1527.50	210.35	14,067.37		
		D	1333.38	268.57	7964.90		
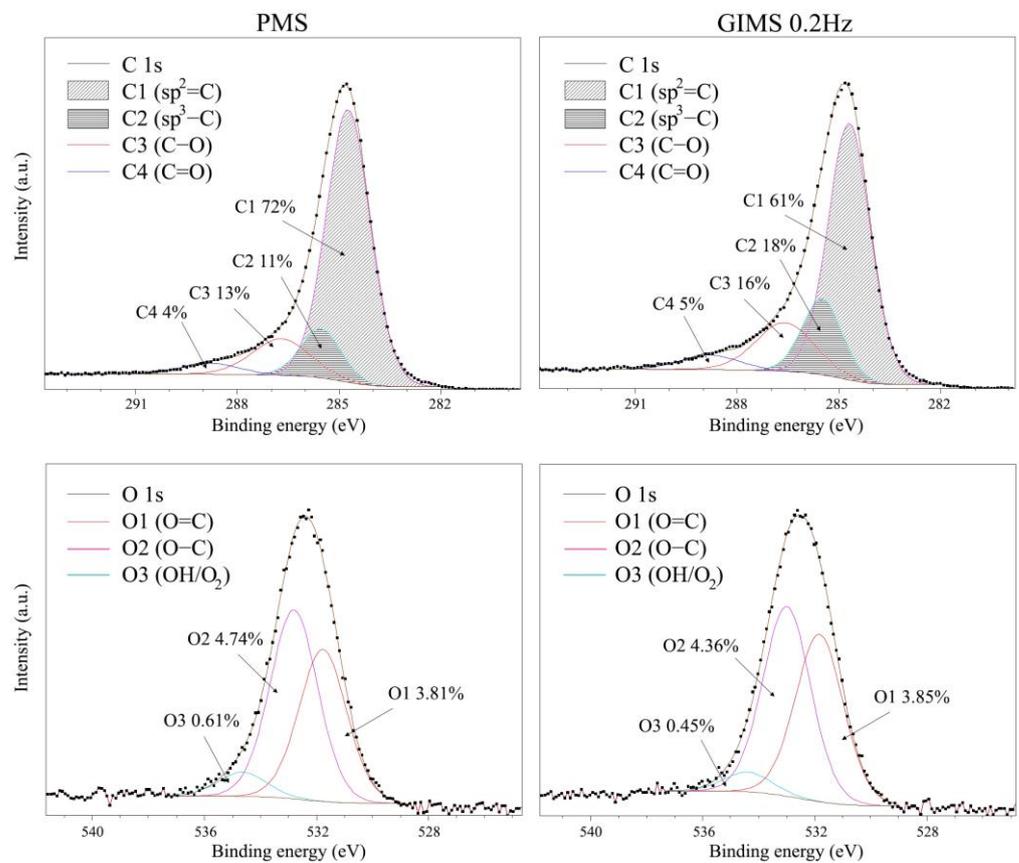
Figure 5. XPS spectra of C1s and O1s orbitals of a-C films fabricated at far conditions of gas dosing: stationary PMS (**left**) and pulsed GIMS 0.2 Hz (**right**).

Table 4. The composition of a-C films determined by X-ray photoelectron spectroscopy.

		C1s (%)			O1s (%)			Concentration (%)	
	C (sp^2)	C (sp^3)	C (C–O)	C (C=O)	O (O–C)	O (O=C)	O (OH)	C	O
PMS	65.20	10.75	11.45	3.44	4.74	3.81	0.61	90.84	9.16
GIMS 0.2 Hz	56.50	15.72	14.72	4.40	4.36	3.85	0.45	91.34	8.66

Figure 6 summarizes the sp^3/sp^2 ratio determined by the two methods. The determined sp^3 contents clearly show the difference between the films fabricated under extreme conditions, PMS and GIMS 0.2 Hz. The difference is almost two-fold in the method of determining the sp^3 by Raman (~20% to ~45%) and XPS (~15% to ~30%). Intermediate GIMS 1 Hz–GIMS 0.25 Hz conditions resulted in films with an sp^3 content in the mid-range values. The differences in the values calculated by the two methods are due to their limitations. The Raman analysis comes from greater depth than the XPS analysis. It is a familiar fact that the XPS typically shows an increased sp^2 content at the surface [51] due to the proposed mechanism of the sp^3 formation in the a-C layers [52]. Nevertheless, the most important conclusion from this part of the experiment is that the conditions most favorable for generating the a-C layers, with elevated $C(sp^3) - C(sp^3)$ bond content, are those of the GIMS process, in which the plasma is generated in a volume characterized by low pressure.

We expected that such conditions are particularly favorable for reducing the energy dispersion of plasma particles into inelastic collisions with cold gas molecules. Studies of the state of the plasma and the magnetron power circuit seem to confirm this. Under the conditions of our experimental apparatus, we obtained a good effect with a gas injection frequency of 0.2 Hz. Under these conditions, the highest energy characterized the discharges and we identified relatively high intensities of OES spectra energetic plasma particles in the plasma composition. The formation of an increased fraction of sp^3 carbon is usually explained in the literature based on Lifshitz's model of subplantation of hyperthermal species [53,54]. This model explains the formation of a diamond-like phase by impinging the graphitic surface by energetic species with energy ranging from 1 to 100 eV. Energetic species can penetrate the crystal lattice shallowly if their energy is enough. Penetration enables atomic displacements and phonon and electron excitations. Excited lattice carbon atoms get extra energy and the possibility of creating local sp^3 hybridization. With an increasing concentration and the kinetic energy of penetrating species, the possibility of forming the sp^3 phase increases. This stays behind the observed trend with decreasing the frequency of gas injections. By increasing the energy of plasma, a plasma source generates a larger population of excited species with higher energy, so a stronger impingement of the substrate in this condition is expected.

In the second part of the experiment, we fabricated the a-C layers using various plasma-forming gases injected at a frequency of 0.2 Hz. As in part one, we aimed to figure out what effect a given gas has on the energy of the generated plasma pulses. The results are shown in Figure 7. Using alternatives to Ar gases and their mixtures increases the plasma pulse energy. This is related to the ionization energies of the individual gases.

The ionization energies of Ne (E_i = 21.56 eV) and He (E_i = 24.58 eV) are higher than Ar (E_i = 15.6 eV). Thanks to this, higher energy is characterized by secondary electrons emitted due to ionization. This directly impacts the efficiency of the sputtering and ionization phenomena. The result is an increase in the population of carbon ions. In the last few years, the literature reports using an alternative for Ar gases to increase the ionization degree of magnetron plasma [55–59].

Figure 8 compares AFM images of the surface topography of the a-C films. The layers deposited in the atmosphere, Ar, Ar + H_2, and Ne, are topographically relatively similar. They are dense and smooth. They exhibit topography features characteristic of a-C layers formed by magnetron sputtering. Films obtained in a mixture with He have a different morphology. They are made of globular particles and their structure is characterized

by relatively high porosity. Such structures are characteristic of coatings produced at relatively high pressures. Structures built of large agglomerates are formed when a small free path of the particles in the plasma characterizes the process. These conditions favor the agglomeration of the phase into larger forms before reaching the substrate. In the case of our experiment, the reasons for this morphology have to be found somewhere else. All layers were produced under the same gas conditions (injection frequency, valve opening time, valve inlet pressure, etc.). The only difference is the presence of He in the mixture.
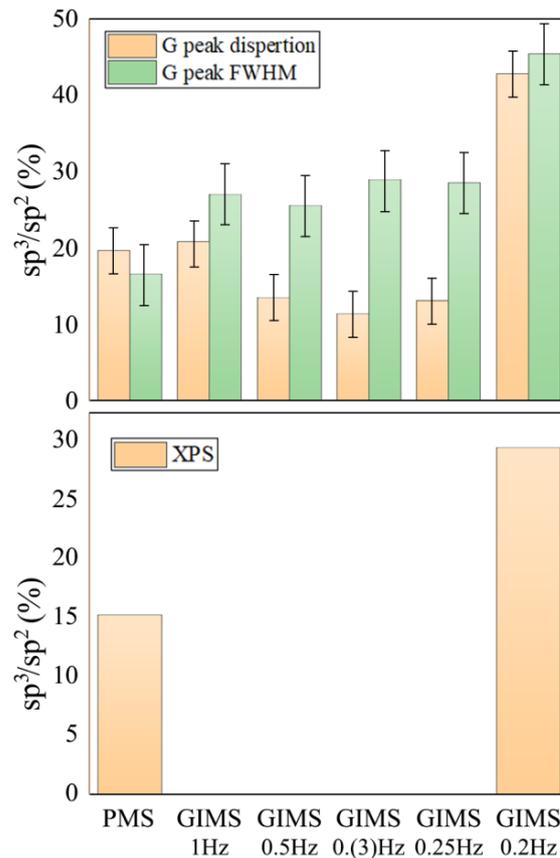
Figure 6. Summarized sp^3/sp^2 ratio determined by Raman spectroscopy (**top**) and XPS (**bottom**).
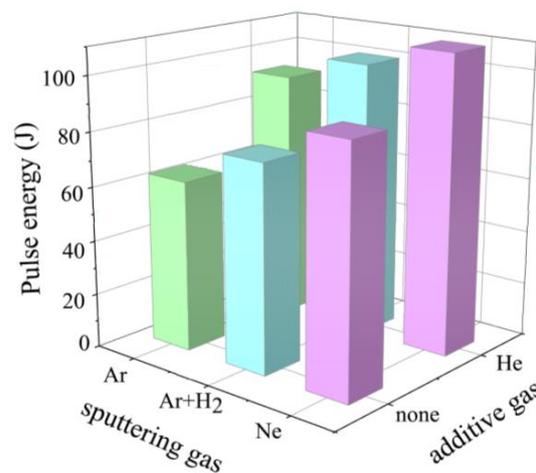
Figure 7. The energy of plasma pulse generated in GIMS under various gases and mixture conditions, calculated by integration of the power characteristics.
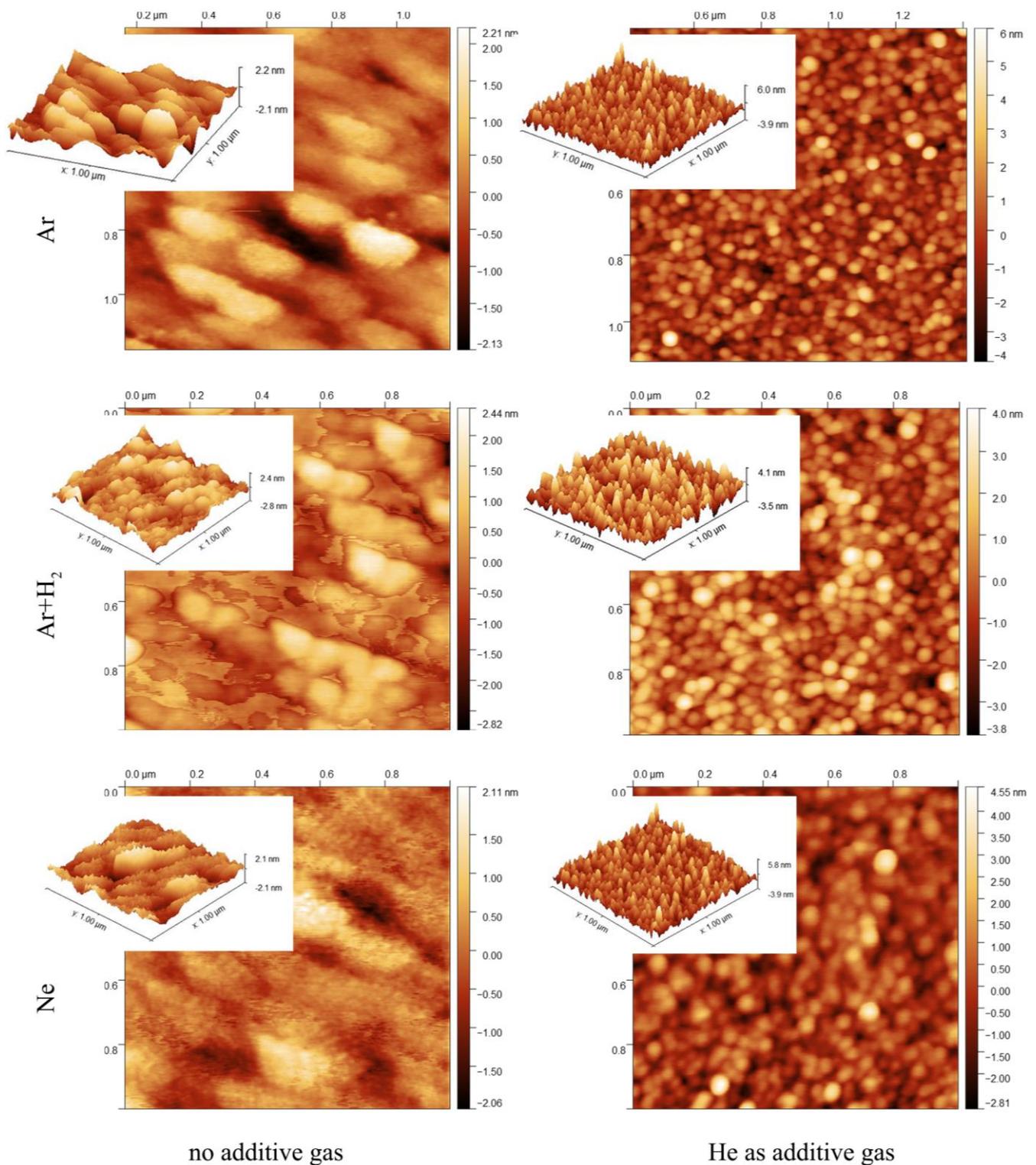
Figure 8. AFM images (top view and 3D view) of a-C films topography deposited in various gas atmospheres.

In our opinion, the so-called cluster-like growth mechanism is behind obtaining such a globular structure. According to Zdunek, homogeneous phase nucleation occurs directly on the plasma ions in the ion-rich plasma, and thermodynamically stable clusters are formed [14,60]. The clusters can undergo agglomeration to form globular forms delivered to the substrate [61]. Particles on the substrate undergo incomplete coalescence phenom-

ena [60]. Particles that undergo incomplete coalescence can be clearly distinguished in the AFM images. Figure 9 shows a series of images showing different stages of coalescence. Coalescence occurs due to the slight diffusive motion of nanoparticles along the surface, and the mechanism of particle aggregation is through mass transport between particles, activated by plasma energy. Coalescence is not complete due to the pulsed nature of the energy distribution.
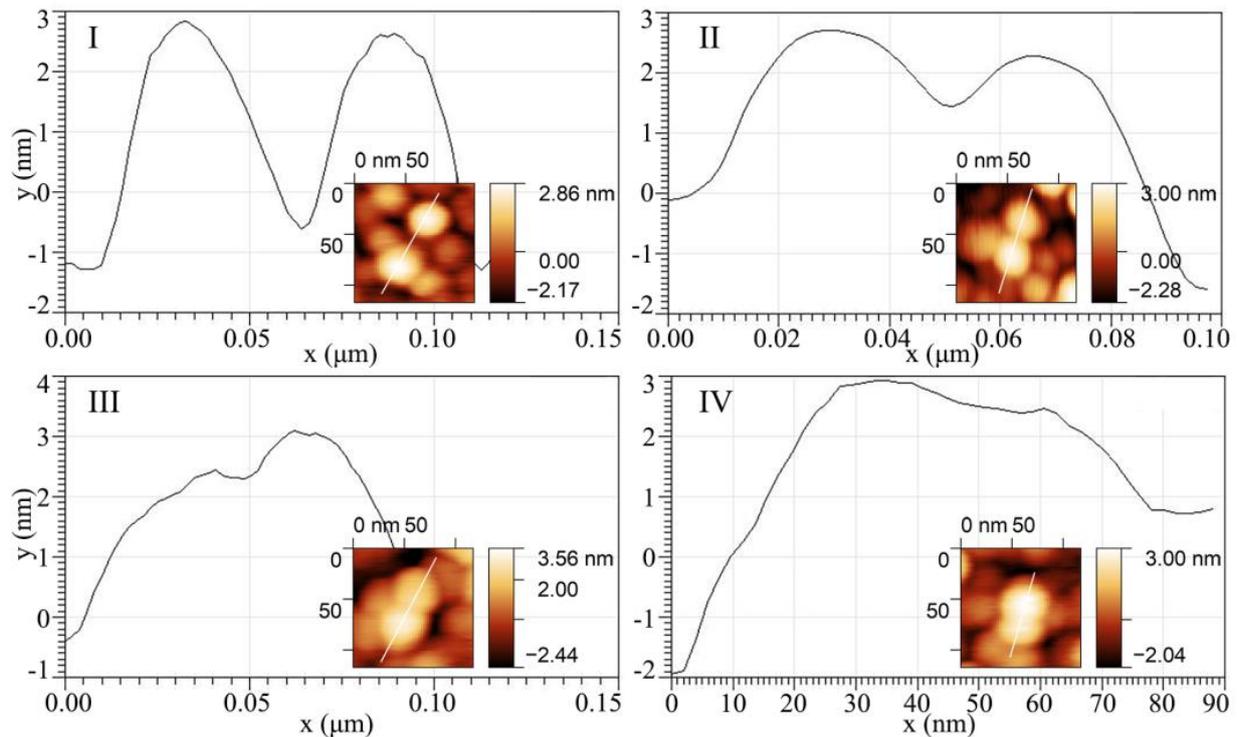
Figure 9. Cross-section analysis of carbon nanoparticles AFM images. Sections ordered in I-IV stages presenting the incomplete coalescence of nanoparticles presented as AFM insets.

A prerequisite for homogeneous nucleation to become apparent over heterogeneous nucleation is increased plasma ionization. Investigations of the energy of glow discharge pulses indicate that the conditions of He in the plasma-forming gas mixture contribute to an increase in the discharge energy. The addition of He resulted in an increase in pulse energy in each case. To confirm this, we recorded the OES spectra of plasma excited under these conditions, and the results of this study are presented in Figure 10. The spectra were presented to compare the effect of the presence of He in the plasma gas mixture. In each case, the addition of He contributes to an increase in the intensity of the emission lines. This includes the excited lines of carbon atoms and ions of the plasma-forming gas.

It should be noted that a strong line of CII carbon ions was identified in the plasma generated in a mixture of Ne and He. In all cases, the intensity of the individual emission lines increases by two orders of magnitude.

Of course, it is not possible on this basis to assess how much the population of excited particles in the plasma increases. Nevertheless, it is possible to conclude that the energy state of the plasma excited in gas with He is increased.

Layers formed in different atmospheres of plasma-forming gases were investigated by XPS chemical analysis. The results of the content of the individual bonds and the determined sp^3/sp^2 ratios are summarized in Figure 11. The detailed composition is presented in Table 5. First, we could not achieve such sp^3 content as in the first part of the experiment.
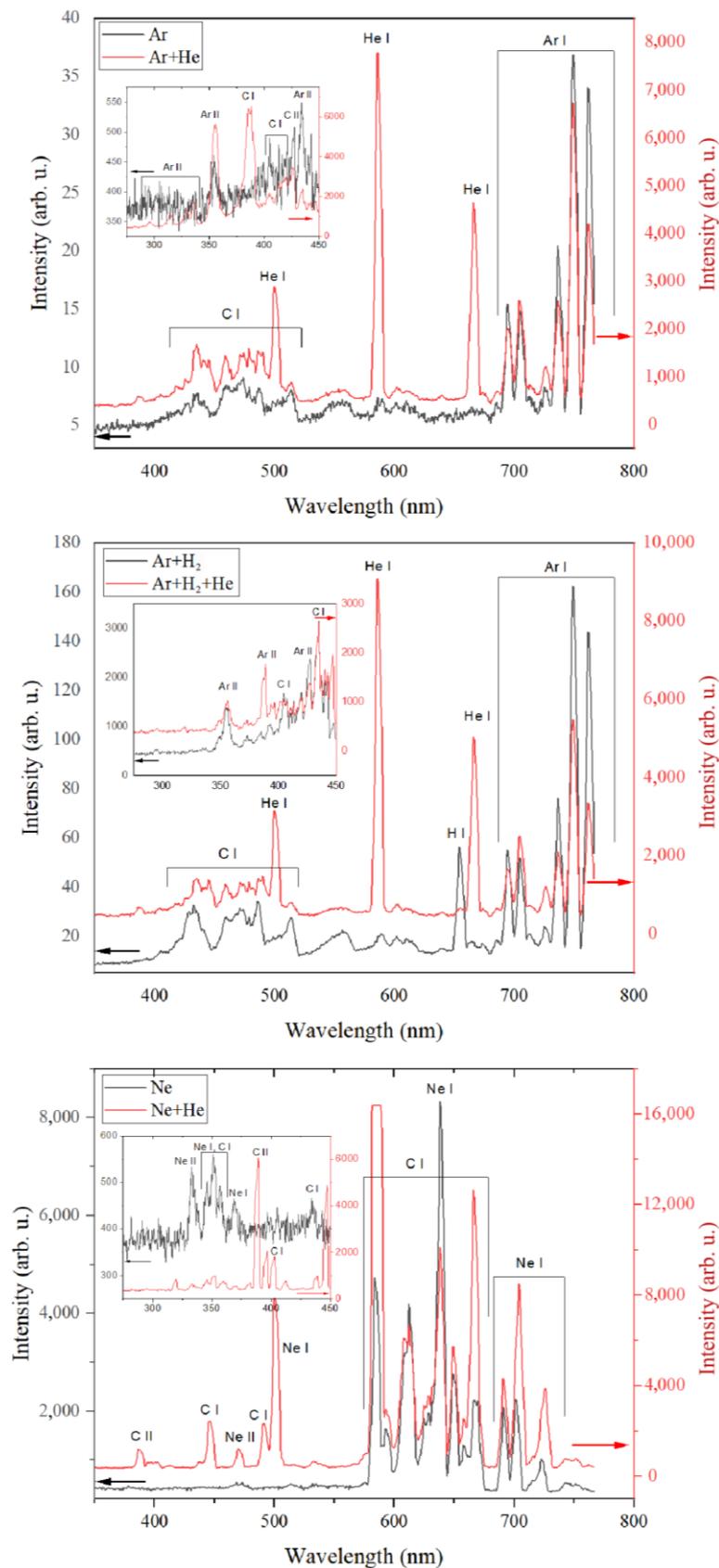
Figure 10. OES spectra of plasma pulses generated in various components of gas mixtures. The spectra measured in the VIS range are presented as large figures. Spectra measured in the UV range are presented as smaller insets.
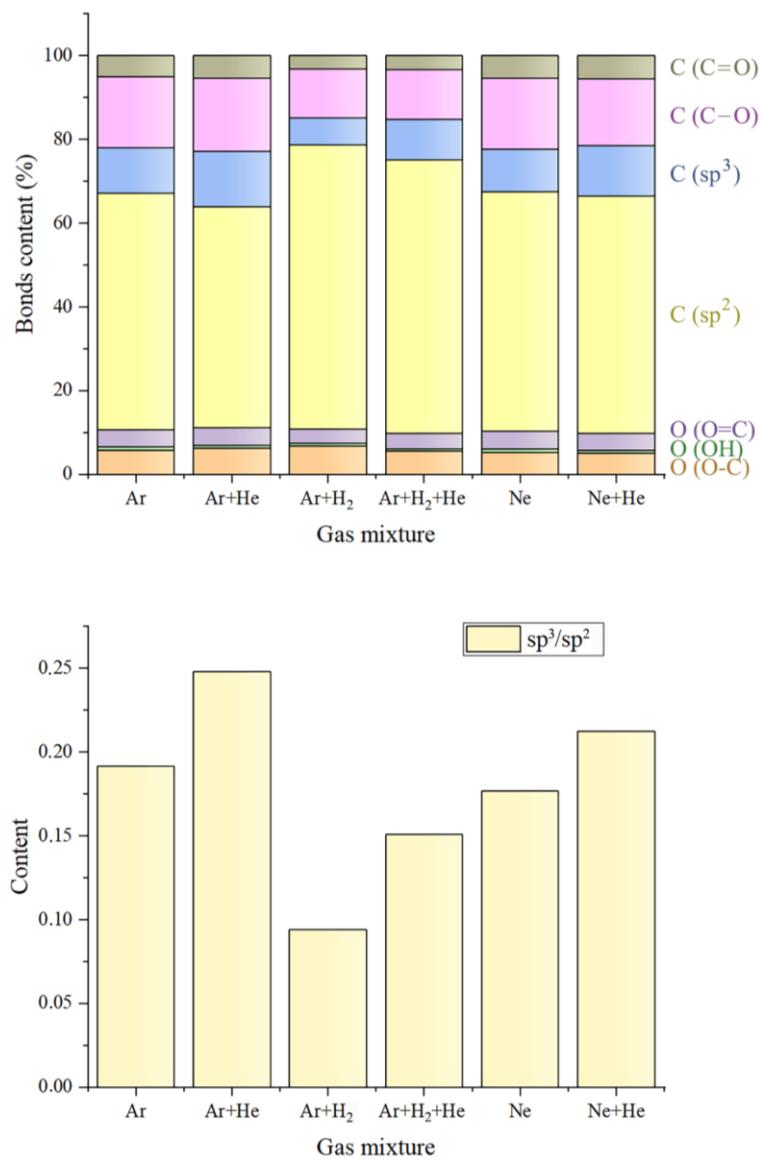
Figure 11. Bonding composition of a-C films deposited in various gas atmospheres and determined by XPS (**top**) and calculated sp^3/sp^2 ratio (**bottom**).

Table 5. The composition of a-C films determined by X-ray photoelectron spectroscopy.

	C 1s (%)				O 1s (%)			Concentration (%)	
	C (sp^2)	C (sp^3)	C (C–O)	C (C=O)	O (O–C)	O (O=C)	O (OH)	C	O
Ar	57.3	10.7	16.5	5.3	5.3	4.0	0.6	89.99	10.01
Ar + He	52.8	13.1	17.5	5.4	6.2	4.1	0.6	88.95	11.05
Ar + H$_2$	67.8	6.3	11.7	3.2	6.7	3.3	0.6	89.21	10.79
Ar + H$_2$ + He	65.2	9.8	11.7	3.4	5.5	3.5	0.6	90.31	9.69
Ne	57.2	10.1	17.0	5.3	5.2	4.3	0.7	89.73	10.27
Ne + He	56.7	12.0	15.8	5.6	5.0	4.0	0.7	90.22	9.78

We believe this is because we had to use two pulse valves to complete the second part of the experiment. With a minimum opening time of 1 ms, the coatings' deposition processes had to be carried out in an atmosphere with twice as much gas, and this caused the negative effect of higher pressure. Although the state of plasma in the individual processes differed significantly, the material effect was not extraordinary. Despite this, the

results show a slight increase in the sp^3 content in mixtures with He. This corresponds well with the previously reported results, which indicated an elevated plasma energy state in the He environment. It is also worth pointing out that using H_2 in the mixture slightly reduced the content of the bonds with oxygen. The presented XPS results show a critical development application for the GIMS technique. There is a clear need for faster pulse valves to produce multi-component gas atmospheres. This is necessary to take advantage of the "genetic" features of GIMS—the advantages of film deposition under low-pressure conditions.

The produced layers were characterized by spectroscopic ellipsometry to characterize the optical properties and to determine the thickness of the produced carbon films. The four medium optical models (from bottom to top: Si\native SiO_2\carbon film\ambient) of a sample were used to obtain the refractive index (n) and the extinction coefficient (k) of the layers. The optical constants of Si and SiO_2 were taken from the database of optical constants [62]. The thickness of the native silicon dioxide was determined in a separate experiment and was established to be 2.5 nm. The complex refractive index $\tilde{n} = n + ik$ of the carbon film was parameterized using a sum of the Gauss-shaped oscillators:

$$\tilde{n}^2 = \varepsilon_\infty + \sum_j \left(A_j, E_j, Br_j\right) \tag{5}$$

where ε_∞ is the high-frequency dielectric constant, while A_j, E_j, and E_j are amplitude, energy, and the broadening of the j-th oscillator. The fit procedure was performed to minimize the standard mean squared error—MSE [63]. The thicknesses of the fabricated a-C films depended on the mixture of the gas used during the sputtering process and were determined to be 96 ± 1 nm (for Ar), 137 ± 1 nm (for Ar + He), 162 ± 1 nm (for Ar + H_2), 148 ± 1 nm (for Ar + H_2 + Ne), 171 ± 1 nm (for Ne), and 98 ± 1 nm (for Ne + He).

The determined refractive index and extinction coefficient (n, k) are given in Figure 12. Layers with a higher $C(sp^3) - C(sp^3)$ bond content are characterized by a higher n above ~500 nm, while below ~500 nm, n is lower. In the NIR spectral range, the refractive index values are at 2.5 for the amorphous carbon films with a higher $C(sp^3) - C(sp^3)$ bond content which decreases to about 2 for the film obtained for the Ar + H_2 mixture of sputtered gas. This sample demonstrates the lowest sp^3 to sp^2 ratio (see Figure 11). The significant decrease in the n spectra for wavelengths shorter than 500 nm is associated with the behavior of the optical response of medium described by the Kramers-Kronig relations [63] of real and imaginary parts of the complex refractive index of the a-C thin films. The absorption features of the deposited carbon films are characterized by the extinction coefficient and absorption spectra (α). As can be seen, the highest spectra values are achieved in the UV and gradually decreases with the increase in the wavelength. The k reaches higher values for the a-C layers with a higher $C(sp^3) - C(sp^3)$ bond content.

In the UV spectral range, the distinct absorption band ($\pi- > \pi^*$ transition) can be visible in the k and α spectra. The lowest amplitude demonstrates the film deposited in the Ar + H_2 mixture (the lowest sp^3/sp^2 ratio), and (generally) increases with the increase in the sp^3 to sp^2 ratio. The TDDFT calculations [62] confirm the behavior of the extinction coefficient/absorption coefficient spectra of the films analyzed in this study. Zoubos et al. show that absorption coefficient values of carbon films with a high (90%) sp^3 content decrease rapidly to zero with the increase in the wavelength. The α decrease is less evident for the layers containing a lower sp^3/sp^2 ratio, and their values are significantly higher than those for the sp^3-rich materials [64]. The deposited a-C layers contain a relatively low content of sp^3 compared to the carbon films described in [64]. Therefore, the determined spectra should be treated as the effective optical response of the synthesized a-C films. Moreover, the absorption threshold cannot be precisely determined because of the lack of a pronounced increase in the k or α.
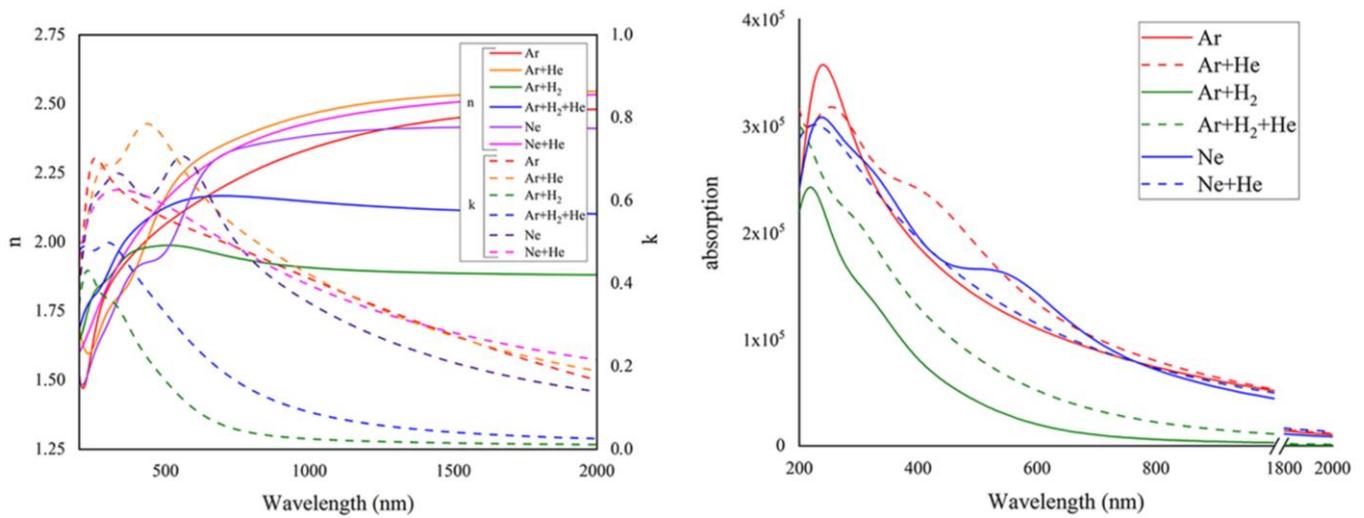
Figure 12. Optical characteristics of a-C coatings: (*n, k*)—left, absorption—right.

The mechanical properties of the a-C films deposited on Si substrates were characterized using nanohardness tests. The results of hardness and reduced Young's modulus measurements using the nanoindentation method are shown in Figure 13. The coatings have a hardness of 8–12 GPa range and a reduced Young's modulus of about 110–160 GPa, which is consistent with the literature results for the a-C layers with a $C(sp^3) - C(sp^3)$ bond content in this range [65–68]. Notably, the summary of the results of the mechanical properties is close to the summary of the sp^3/sp^2 ratio shown in Figure 11. This confirms the general knowledge of how much the mechanical properties of carbon films are related to the content of the $C(sp^3) - C(sp^3)$ bonds.
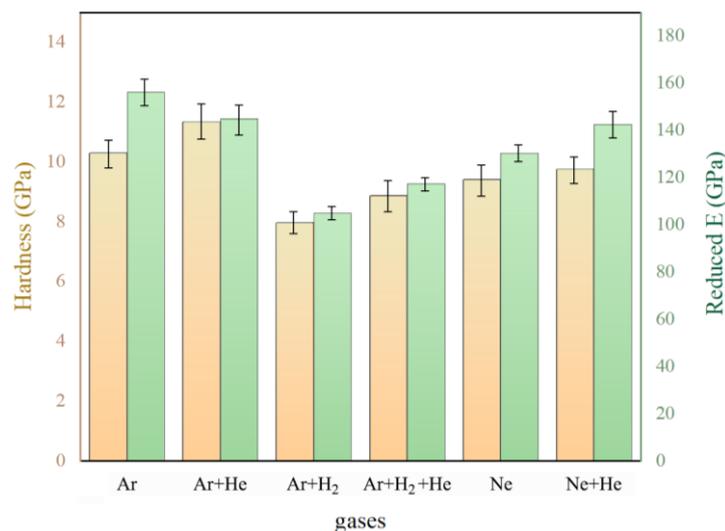
Figure 13. Mechanical properties of a-C films expressed by nano hardness and reduced Young modulus.

4. Conclusions

This work presented the GIMS technique in the context of the a-C coatings synthesis. The pulsed plasma generated by the injections of a small portion of gas may contribute to preserving the kinetic energy of plasma species. This preservation of the energy is provided when the system, quickly evacuating the cold gas volume, is used. In the GIMS technique, this can be achieved by decreasing the frequency of gas injections. OES investigation proved that plasma generated in this condition consists of more energetic constituents than plasma created in stationary conditions. The plasma emission spectra were compared

with the phase structure of the a-C films. In the films fabricated under more energetic plasma conditions, a higher content of the $C(sp^3) - C(sp^3)$ bonds was identified. Using our GIMS experimental setup, we achieved an sp^3/sp^2 ratio of ~45%. This is not a result that is achieved by methods such as filtered arc deposition, ion beam deposition, or PECVD methods, where one can approach 90% with the $C(sp^3) - C(sp^3)$ bonds content. We consider our result relatively good, considering that the magnetron sputtering process, in its standard version of power distribution and without substrate polarization, can rarely achieve such values. Only the high-power variant HiPIMS, which additionally uses substrate polarization successfully, exceeds such values. However, it should be noted that the GIMS technique in our experiment used a standard power source. All the results presented in this paper seem consistent and lead to the conclusion that controlling the magnetron plasma, using gas pulses, can be considered a suitable method for optimizing the features of the deposited material in the form of coating.

Moreover, the low–frequency GIMS shows features of a process that uses electric energy more effectively to form the coating material. The second approach used to increase the energy state of the plasma was to use alternative gases. The use of gases with higher ionization energy than argon brings good results. In these cases, we observed discharges with high energies, and the plasma spectrum was enriched with sputtering products and ions. In particular, it seems that He, as an additive to the plasma-forming mixture, is particularly beneficial. Its use resulted in a higher sp^3/sp^2 ratio and a slightly different film growth mechanism, characteristic of ion-rich nucleation conditions.

Institutional Review Board Statement: Not applicable.

Informed Consent Statement: Not applicable.

Data Availability Statement: Not applicable.

Conflicts of Interest: The authors declare no conflict of interest.

References

1. Robertson, J. Diamond-like amorphous carbon. *Mater. Sci. Eng. R Rep.* **2002**, *37*, 129–281. [CrossRef]
2. Zhang, L.; Wei, X.; Lin, Y.; Wang, F. A ternary phase diagram for amorphous carbon. *Carbon* **2015**, *94*, 202–213. [CrossRef]
3. Huang, J.; Wang, L.; Liu, B.; Wan, S.; Xue, Q. In Vitro Evaluation of the Tribological Response of Mo-Doped Graphite-like Carbon Film in Different Biological Media. *ACS Appl. Mater. Interfaces* **2015**, *7*, 2772–2783. [CrossRef]
4. Gupta, B.K.; Bhushan, B. Micromechanical properties of amorphous carbon coatings deposited by different deposition techniques. *Thin Solid Film.* **1995**, *270*, 391–398. [CrossRef]
5. Neuville, S. New application perspective for tetrahedral amorphous carbon coatings. *QScience Connect* **2014**, *2014*, 8. [CrossRef]
6. Donnet, C.; Fontaine, J.; le Mogne, T.; Belin, M.; Héau, C.; Terrat, J.P.; Vaux, F.; Pont, G. Diamond-like carbon-based functionally gradient coatings for space tribology. *Surf. Coat. Technol.* **1999**, *120–121*, 548–554. [CrossRef]
7. Risplendi, F.; Bernardi, M.; Cicero, G.; Grossman, J.C. Structure-property relations in amorphous carbon for photovoltaics. *Appl. Phys. Lett.* **2014**, *105*, 043903. [CrossRef]
8. Kim, I.; Shim, C.; Kim, S.W.; Lee, C.; Kwon, J.; Byun, K.; Jeong, U. Amorphous Carbon Films for Electronic Applications. *Adv. Mater.* **2022**, 2204912. [CrossRef]
9. Patsalas, P. Optical properties of amorphous carbons and their applications and perspectives in photonics. *Thin Solid Film.* **2011**, *519*, 3990–3996. [CrossRef]
10. Dhandapani, V.S.; Subbiah, R.; Thangavel, E.; Arumugam, M.; Park, K.; Gasem, Z.M.; Veeraragavan, V.; Kim, D.-E. Tribological properties, corrosion resistance and biocompatibility of magnetron sputtered titanium-amorphous carbon coatings. *Appl. Surf. Sci.* **2016**, *371*, 262–274. [CrossRef]

11. Liu, E.; Shi, X.; Tay, B.K.; Cheah, L.K.; Tan, H.S.; Shi, J.R.; Sun, Z. Micro-Raman spectroscopic analysis of tetrahedral amorphous carbon films deposited under varying conditions. *J. Appl. Phys.* **1999**, *86*, 6078–6083. [CrossRef]

12. Xu, S.; Tay, B.K.; Tan, H.S.; Zhong, L.; Tu, Y.Q.; Silva, S.R.P.; Milne, W.I. Properties of carbon ion deposited tetrahedral amorphous carbon films as a function of ion energy. *J. Appl. Phys.* **1996**, *79*, 7234–7240. [CrossRef]

13. Jiang, Q.; Chen, Z.P. Thermodynamic phase stabilities of nanocarbon. *Carbon* **2006**, *44*, 79–83. [CrossRef]

14. Sokolowski, M.; Sokolowska, A. Electric charge influence on the metastable phase nucleation. *J. Cryst. Growth* **1982**, *57*, 185–188. [CrossRef]

15. Hwang, N.M.; Yoon, D.Y. Thermodynamic approach to the paradox of diamond formation with simultaneous graphite etching in the low pressure synthesis of diamond. *J. Cryst. Growth* **1996**, *160*, 98–103. [CrossRef]

16. Liu, H.; Dandy, D.S. Studies on nucleation process in diamond CVD: An overview of recent developments. *Diam. Relat. Mater.* **1995**, *4*, 1173–1188. [CrossRef]

17. Gudmundsson, J.T.; Lundin, D. Introduction to magnetron sputtering. In *High Power Impulse Magnetron Sputtering*; Elsevier: Amsterdam, The Netherlands, 2020; pp. 1–48. [CrossRef]

18. Rossnagel, S.M. Magnetron sputtering. *J. Vac. Sci. Technol. A* **2020**, *38*, 060805. [CrossRef]

19. Petrov, I.; Myers, A.; Greene, J.E.; Abelson, J.R. Mass and energy resolved detection of ions and neutral sputtered species incident at the substrate during reactive magnetron sputtering of Ti in mixed Ar+N$_2$ mixtures. *J. Vac. Sci. Technol. A Vac. Surf. Film.* **1994**, *12*, 2846–2854. [CrossRef]

20. Christou, C.; Barber, Z.H. Ionization of sputtered material in a planar magnetron discharge. *J. Vac. Sci. Technol. A Vac. Surf. Film.* **2000**, *18*, 2897–2907. [CrossRef]

21. Huang, M.; Zhang, X.; Ke, P.; Wang, A. Graphite-like carbon films by high power impulse magnetron sputtering. *Appl. Surf. Sci.* **2013**, *283*, 321–326. [CrossRef]

22. Crespi, Â.E.; Ballage, C.; Hugon, M.C.; Robert, J.; Lundin, D.; Vickridge, I.; Alvarez, J.; Minea, T. Low resistivity amorphous carbon-based thin films employed as anti-reflective coatings on copper. *Thin Solid Film.* **2020**, *712*, 138319. [CrossRef]

23. Greczynski, G.; Lu, J.; Jensen, J.; Bolz, S.; Kölker, W.; Schiffers Ch Lemmer, O.; Greene, J.E.; Hultman, L. A review of metal-ion-flux-controlled growth of metastable TiAlN by HIPIMS/DCMS co-sputtering. *Surf. Coat. Technol.* **2014**, *257*, 15–25. [CrossRef]

24. Minea, T.M.; Costin, C.; Revel, A.; Lundin, D.; Caillault, L. Kinetics of plasma species and their ionization in short-HiPIMS by particle modeling. *Surf. Coat. Technol.* **2014**, *255*, 52–61. [CrossRef]

25. Lundin, D.; Čada, M.; Hubička, Z. Ionization of sputtered Ti, Al, and C coupled with plasma characterization in HiPIMS. *Plasma Sources Sci. Technol.* **2015**, *24*, 035018. [CrossRef]

26. Lin, J.; Sproul, W.D.; Wei, R.; Chistyakov, R. Diamond like carbon films deposited by HiPIMS using oscillatory voltage pulses. *Surf. Coat. Technol.* **2014**, *258*, 1212–1222. [CrossRef]

27. Sarakinos, K.; Braun, A.; Zilkens, C.; Mráz, S.; Schneider, J.M.; Zoubos, H.; Patsalas, P. Exploring the potential of high power impulse magnetron sputtering for growth of diamond-like carbon films. *Surf. Coat. Technol.* **2012**, *206*, 2706–2710. [CrossRef]

28. Lattemann, M.; Abendroth, B.; Moafi, A.; McCulloch, D.G.; McKenzie, D.R. Controlled glow to arc transition in sputtering for high rate deposition of carbon films. *Diam. Relat. Mater.* **2011**, *20*, 68–74. [CrossRef]

29. Hiratsuka, M.; Azuma, A.; Nakamori, H.; Kogo, Y.; Yukimura, K. Extraordinary deposition rate of diamond-like carbon film using HIPIMS technology. *Surf. Coat. Technol.* **2013**, *229*, 46–49. [CrossRef]

30. Santiago, J.A.; Fernández-Martínez, I.; Wennberg, A.; Molina-Aldareguia, J.M.; Castillo-Rodríguez, M.; Rojas, T.C.; Sánchez-López, J.C.; González, M.U.; García-Martín, J.M.; Li, H.; et al. Adhesion enhancement of DLC hard coatings by HiPIMS metal ion etching pretreatment. *Surf. Coat. Technol.* **2018**, *349*, 787–796. [CrossRef]

31. Chodun, R.; Nowakowska-Langier, K.; Wicher, B.; Okrasa, S.; Kwiatkowski, R.; Zaloga, D.; Dypa, M.; Zdunek, K. The state of coating–substrate interfacial region formed during TiO2 coating deposition by Gas Injection Magnetron Sputtering technique. *Surf. Coat. Technol.* **2020**, *398*, 126092. [CrossRef]

32. Chodun, R.; Nowakowska-Langier, K.; Wicher, B.; Okrasa, S.; Minikayev, R.; Dypa, M.; Zdunek, K. TiO$_2$ coating fabrication using gas injection magnetron sputtering technique by independently controlling the gas and power pulses. *Thin Solid Film.* **2021**, *728*, 138695. [CrossRef]

33. Chodun, R.; Skowronski, L.; Okrasa, S.; Wicher, B.; Nowakowska-Langier, K.; Zdunek, K. Optical TiO$_2$ layers deposited on polymer substrates by the Gas Injection Magnetron Sputtering technique. *Appl. Surf. Sci.* **2019**, *466*, 12–18. [CrossRef]

34. Wicher, B.; Chodun, R.; Trzcinski, M.; Lachowski, A.; Nowakowska-Langier, K.; Ibrahim, S.H.; Jaroszewicz, J.; Kubiś, M.; Grzanka, E.; Zdunek, K. Application of the plasma surface sintering conditions in the synthesis of ReBx–Ti targets employed for hard films deposition in magnetron sputtering technique. *Int. J. Refract. Met. Hard Mater.* **2022**, *103*, 105756. [CrossRef]

35. Wicher, B.; Chodun, R.; Trzciński, M.; Lachowski, A.; Kubiś, M.; Nowakowska-Langier, K.; Zdunek, K. Design of pulsed neon injection in the synthesis of W-B-C films using magnetron sputtering from a surface-sintered single powder cathode. *Thin Solid Film.* **2020**, *716*, 138426. [CrossRef]

36. Wicher, B.; Chodun, R.; Kwiatkowski, R.; Trzcinski, M.; Nowakowska–Langier, K.; Lachowski, A.; Minikayev, R.; Rudnicki, J.; Naparty, M.K.; Zdunek, K. Plasmochemical investigations of DLC/WCx nanocomposite coatings synthesized by gas injection magnetron sputtering technique. *Diam. Relat. Mater.* **2019**, *96*, 1–10. [CrossRef]

37. Skowronski, L.; Zdunek, K.; Nowakowska-Langier, K.; Chodun, R.; Trzcinski, M.; Kobierski, M.; Kustra, M.K.; Wachowiak, A.A.; Wachowiak, W.; Hiller, T.; et al. Characterization of microstructural, mechanical and optical properties of TiO$_2$ layers deposited by GIMS and PMS methods. *Surf. Coat. Technol.* **2015**, *282*, 16–23. [CrossRef]

38. Wicher, B.; Chodun, R.; Trzcinski, M.; Nowakowska-Langier, K.; Skowroński, Ł.; Lachowski, A.; Zdunek, K. Applications insight into the plasmochemical state and optical properties of amorphous CNx films deposited by gas injection magnetron sputtering method. *Appl. Surf. Sci.* **2021**, *565*, 150540. [CrossRef]

39. Wicher, B.; Chodun, R.; Nowakowska-Langier, K.; Trzcinski, M.; Skowroński, L.; Okrasa, S.; Minikayev, R.; Naparty, M.K.; Zdunek, K. Chemical and structural characterization of tungsten nitride (WNx) thin films synthesized via Gas Injection Magnetron Sputtering technique. *Vacuum* **2019**, *165*, 266–273. [CrossRef]

40. Zdunek, K.; Skowroński, L.; Chodun, R.; Nowakowska-Langier, K.; Grabowski, A.; Wachowiak, W.; Okrasa, S.; Wachowiak, A.; Strauss, O.; Wronkowski, A.; et al. Novel GIMS technique for deposition of colored Ti/TiO$_2$ coatings on industrial scale. *Mater. Sci.-Pol.* **2016**, *34*, 137–141. [CrossRef]

41. Skowronski, L.; Chodun, R.; Zdunek, K. TiO$_2$—Based decorative interference coatings produced at industrial conditions. *Thin Solid Film.* **2020**, *711*, 138294. [CrossRef]

42. Gencoa Ltd. Gencoa: Balanced and Unbalanced. Available online: https://www.gencoa.com/balance-unbalance (accessed on 23 March 2023).

43. Pawlak, W.; Jakubowska, M.; Sobczyk-Guzenda, A.; Makówka, M.; Szymanowski, H.; Wendler, B.; Gazicki-Lipman, M. Photo activated performance of titanium oxide coatings deposited by reactive gas impulse magnetron sputtering. *Surf. Coat. Technol.* **2018**, *349*, 647–654. [CrossRef]

44. Posadowski, W.M.; Wiatrowski, A.; Dora, J.; Radzimski, Z.J. Magnetron sputtering process control by medium-frequency power supply parameter. *Thin Solid Film.* **2008**, *516*, 4478–4482. [CrossRef]

45. Dora, J. Resonant Power Supply. Patent No. 313150, 6 March 1996.

46. Cui, W.G.; Lai, Q.B.; Zhang, L.; Wang, F.M. Quantitative measurements of sp^3 content in DLC films with Raman spectroscopy. *Surf. Coat. Technol.* **2010**, *205*, 1995–1999. [CrossRef]

47. Streletskiy, O.; Perevedentseva, E.; Zavidovskiy, I.; Karmenyan, A.; Sychev, V.; Sadykova, V.; Kuvarina, A.; Cheng, C.-L. Amorphous Carbon Films with Embedded Well-Dispersed Nanodiamonds: Plasmon-Enhanced Analysis and Possible Antimicrobial Applications. *Magnetochemistry* **2022**, *8*, 171. [CrossRef]

48. Zavidovskiy, I.A.; Streletskiy, O.A.; Nishchak, O.Y.; Haidarov, A.A.; Pavlikov, A.V. The influence of ion assistance energy on structural and optical properties of carbon-silver nanocomposites. *Thin Solid Film.* **2021**, *738*, 138966. [CrossRef]

49. Ferrari, A.C.; Libassi, A.; Tanner, B.K.; Stolojan, V.; Yuan, J.; Brown, L.M.; Rodil, S.E.; Kleinsorge, B.; Robertson, J. Density, sp^3 fraction, and cross-sectional structure of amorphous carbon films determined by x-ray reflectivity and electron energy-loss spectroscopy. *Phys. Rev. B* **2000**, *62*, 11089–11103. [CrossRef]

50. Tuinstra, F.; Koenig, J.L. Raman Spectrum of Graphite. *J. Chem. Phys.* **1970**, *53*, 1126–1130. [CrossRef]

51. Streletskiy, O.A.; Zavidovskiy, I.A.; Balabanyan, V.Y.; Tsiskarashvili, A.V. Antibacterial properties of modified a-C and ta-C coatings: The effects of the sp^2/sp^3 ratio, oxidation, nitridation, and silver incorporation. *Appl. Phys. A* **2022**, *128*, 929. [CrossRef]

52. Caro, M.A.; Deringer, V.L.; Koskinen, J.; Laurila, T.; Csányi, G. Growth Mechanism and Origin of High sp^3 Content in Tetrahedral Amorphous Carbon. *Phys. Rev. Lett.* **2018**, *120*, 166101. [CrossRef]

53. Lifshitz, Y.; Kasi, S.R.; Rabalais, J.W. Mass selected ion beam deposition: A tool for parametric growth studies, process development and fabrication of diamondlike films. *Adv. Mater. Manuf. Process.* **1988**, *3*, 157–194. [CrossRef]

54. Lifshitz, Y.; Kasi, S.R.; Rabalais, J.W. Subplantation model for film growth from hyperthermal species: Application to diamond. *Phys. Rev. Lett.* **1989**, *62*, 1290–1293. [CrossRef] [PubMed]

55. Aijaz, A.; Sarakinos, K.; Lundin, D.; Brenning, N.; Helmersson, U. A strategy for increased carbon ionization in magnetron sputtering discharges. *Diam. Relat. Mater.* **2012**, *23*, 1–4. [CrossRef]

56. Aijaz, A.; Louring, S.; Lundin, D.; Kubart, T.; Jensen, J.; Sarakinos, K.; Helmersson, U. Synthesis of hydrogenated diamondlike carbon thin films using neon–acetylene based high power impulse magnetron sputtering discharges. *J. Vac. Sci. Technol. A Vac. Surf. Film.* **2016**, *34*, 061504. [CrossRef]

57. Akhavan, B.; Ganesan, R.; Matthews, D.T.A.; McKenzie, D.R.; Bilek, M.M.M. Noble gas control of diamond-like content and compressive stress in carbon films by arc-mixed mode high power impulse magnetron sputtering. *Surf. Coat. Technol.* **2021**, *427*, 127785. [CrossRef]

58. Wicher, B.; Chodun, R.; Skowroński, Ł.; Trzcinski, M.; Kulikowski, K.; Zdunek, K. Design of thin DLC/TiO$_2$ film interference coatings on glass screen protector using a neon–argon-based gas injection magnetron sputtering technique. *Diam. Relat. Mater.* **2022**, *123*, 108859. [CrossRef]

59. Zeb, S.; Qayyum, A.; Sadiq, M.; Shafiq, M.; Waheed, A.; Zakaullah, M. Deposition of Diamond-like Carbon Films using Graphite Sputtering in Neon Dense Plasma. *Plasma Chem. Plasma Process.* **2007**, *27*, 127–139. [CrossRef]

60. Zdunek, K. Concept, techniques, deposition mechanism of impulse plasma deposition—A short review. *Surf. Coat. Technol.* **2007**, *201*, 4813–4816. [CrossRef]

61. Nowakowska-Langier, K.; Chodun, R.; Nietubyc, R.; Minikayev, R.; Zdunek, K. Dependence of the specific features of two PAPVD methods: Impulse Plasma Deposition (IPD) and Pulsed Magnetron Sputtering (PMS) on the structure of Fe–Cu alloy layers. *Appl. Surf. Sci.* **2013**, *275*, 14–18. [CrossRef]

62. JA Woollam Co. Inc. *Guide to Using WVASE32*; Wextech Systems; JA Woollam Co., Inc.: Lincoln, NE, USA, 2010.
63. Fujiwara, H. *Spectroscopic Ellipsometry. Principles and Applications*; John Wiley and Sons: Hoboken, NJ, USA, 2009.
64. Zoubos, H.; Koutsokeras, L.E.; Anagnostopoulos, D.F.; Lidorikis, E.; Kalogirou, S.A.; Wildes, A.R.; Kelires, P.C.; Patsalas, P. Broadband optical absorption of amorphous carbon/Ag nanocomposite films and its potential for solar harvesting applications. *Sol. Energy Mater. Sol. Cells* **2013**, *117*, 350–356. [CrossRef]
65. Dai, H.Y.; Zhan, C.; Du, J. Studies on the influence of sputtering power on amorphous carbon films deposited by pulsed unbalanced magnetron sputtering. *Optik* **2016**, *127*, 2512–2515. [CrossRef]
66. Dai, H.Y.; Du, J.; Zhan, C. Role of target-substrate distance on the structural, mechanical and electrical properties of amorphous carbon films. *J. Mater. Sci. Mater. Electron.* **2015**, *26*, 6552–6556. [CrossRef]
67. Radek, N.; Pietraszek, J.; Szczotok, A.; Fabian, P.; Kalinowski, A. Microstructure and Tribological Properties of DLC Coatings. *Terotechnology* **2020**, *XI*, 171–176. [CrossRef]
68. Jatti, V.S.; Laad, M.; Singh, T.P. Raman Spectroscopy Studies on DLC Films Synthesized by PECVD Method. *Appl. Mech. Mater.* **2014**, *592–594*, 842–846. [CrossRef]